Flow through rotating straight pipes

U. Lei and C. H. Hsu
Institute of Applied Mechanics, National Taiwan University, Taipei 10764, Taiwan, Republic of China

(Received 16 November 1988; accepted 21 September 1989)

Detailed numerical simulation has been carried out for fully developed laminar flow through a circular straight pipe with radius a, which is rotating with constant speed Ω about an axis perpendicular to its own axis. The flow is symmetric about a plane containing the pipe axis with its normal parallel to the rotation axis. There are four types of flow regime that result from the various effects of the secondary flow on the main stream via the convection and Coriolis term. When $R_\Omega \leqslant 10$ and $R_\Omega G \leqslant 100$, the axial velocity profile is essentially axisymmetric and parabolic. Here $R_\Omega = \Omega a^2/\nu$ and $G = G^* a^3/(\rho\nu^2)$, where G^* is the reduced axial pressure gradient driving the flow, ρ is the fluid density, and ν is the kinematic viscosity. When $R_\Omega < 0.85(R_\Omega G)^{1/3}$ and $R_\Omega G > 100$, the axial velocity profile is skewed toward the pressure side with one maximum occurring on the symmetric plane. When $R_\Omega > 1.26(R_\Omega G)^{2/5}$ and $R_\Omega > 10$, the axial velocity shows a dumbell-like profile with the "dumbell" center coinciding with the pipe axis and the "dumbell" axis perpendicular to the symmetric plane. When $0.85(R_\Omega G)^{1/3} \leqslant R_\Omega \leqslant 1.26(R_\Omega G)^{2/5}$ and $R_\Omega G > 100$, the axial velocity profile is skewed toward the pressure size but with two maxima, occurring symmetrically on both sides of the symmetric plane. The present calculation bridges most of the previous asymptotic analyses and provides a correlation formula for the friction factor ratio between the rotating and stationary pipe flow for most of the laminar regime of engineering interest.

I. INTRODUCTION

The secondary flow driven by the centrifugal force in a curved pipe has been studied extensively, as shown in the review paper by Berger *et al.*[1] Here we study another type of secondary flow driven by the Coriolis force in a rotating frame. Consider a fluid flowing through a circular straight pipe with radius a that is rotating at a constant angular velocity $-\Omega\hat{j}$ about an axis perpendicular to its own axis (see Fig. 1). Let (r',θ,z') be the rotating cylindrical coordinates moving with the pipe wall and (u',v',w') be their corresponding velocity components. Also, let (x',y',z') be the Cartesian coordinates corresponding to (r',θ,z'). The primary flow along the z' axis is maintained by an imposed axial pressure gradient $-\partial p'/\partial z'$. The secondary flow is set up in the $r'\theta$ plane by the Coriolis force through its interaction with the viscous force and the pressure term in the r' and θ directions. The secondary flow starts from $\theta = 0$ and separates into two streams: one along the upper wall and one along the lower wall. These two streams collide at $\theta = \pi$ and form a return flow across the core region. The flow is symmetric about the plane $y' = 0$. In the present study, we restrict ourselves to laminar fully developed cases with gravity $\mathbf{g}$ in the y' direction. The flow field is characterized by two independent dimensionless parameters: R_Ω^2 and $R_\Omega G$, where $R_\Omega = \Omega a^2/\nu$ is the rotational Reynolds number and $G = (G^* a^3)/(\rho\nu^2)$. Here $G^* = -\partial p'/\partial z' + \rho\Omega^2 z'$ is a constant for fully developed flow, ρ is the fluid density, and ν is the kinematic viscosity. Both ρ and ν will be taken to be constants in the following analysis. The Reynolds number based on the axial mean velocity w'_m defined by $R = w'_m a/\nu$ is also a suitable dimensionless parameter in characterizing the flow field. The relationship among R_Ω, G, and R will be derived in the next section. Other dimensionless groups of interests, including those employed by the previous investigators, can be derived from either two of these three dimensionless parameters.

Baura[2] and Benton[3] considered the present problem for small R_Ω and hence were able to carry out a regular perturbation solution for the Hagen–Poiseuille flow. Later, Benton and Boyer[4] studied the case for $R_\Omega \gg 1$ and $R_\Omega \gg R$. They found that the core flow is geostrophic and the viscous effects are confined to the thin boundary layer next to the pipe wall. Ito and Nanbu[5] investigated both the laminar and turbulent cases experimentally for wide ranges of parameters and obtained correlations for the friction factor ratio between the rotating and stationary straight pipes. They also carried out a theoretical analysis for laminar flow when $R \gg R_\Omega$, $RR_\Omega \gg 1$ and $R_\Omega \gg R$, $R_\Omega \gg 1$ by the integral method.

Duck[6] studied the problem numerically by using a Fourier decomposition method for $R_\Omega = O(1)$ and $R_\Omega G = O(10^3)$–$O(10^5)$. Berman and Mockros[7] obtained a third-order regular perturbation solution for small parameter N_α ($= R_\Omega/48$ here) for flow in a rotating nonaligned straight pipe. Their solution includes cases when the rotation axis makes an angle $\alpha (0 < \alpha < 90°)$ with the pipe axis, and is expressed in terms of two dimensionless parameters: N_α^2 ($= R_\Omega^2/2304$) and $N_R N_\alpha$ ($= R_\Omega R/24$). They found that there exist three types of flow regime depending on the relative magnitudes of the parameters $N_R N_\alpha$ and N_α^2. In the regime where N_α^2 is small but $N_R N_\alpha$ is not, the effect of rotation is to skew the parabolic axial velocity profile (Hagen–Posieuille) toward the outside, i.e., rotation moves the location of maximum axial velocity outward along $\theta = 0°$ in Fig. 1. In the regime where $N_R N_\alpha$ is small but N_α^2 is not, the effect of rotation is to reduce the centerline velocity

 0899-8213/90/010063-13$02.00

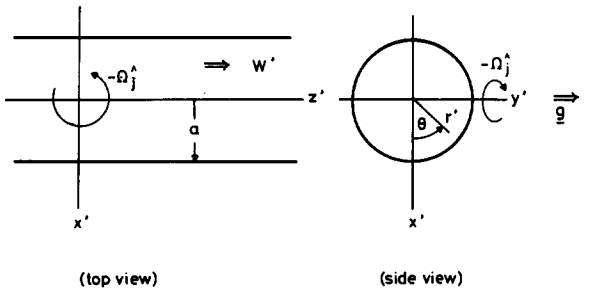

FIG. 1. Configuration of the flow system.

and produce an axial velocity profile with two maxima, one along $\theta = 90°$ and one along $\theta = 270°$. If both $N_R N_\alpha$ and N_α^2 are of significant size, the axial velocity profile is skewed with two maxima. Mansour[8] reconsidered the low R_Ω case studied by Baura[2] and Benton.[3] He expanded the series solution in terms of a single similarity parameter K (proportional to $R_\Omega G$ here) up to 34 terms by computer, and found that the friction factor ratio between the rotating and stationary pipe grows asymptotically as the $\frac{1}{8}$ powers of K and not as the $\frac{1}{4}$ power obtained previously by Ito and Nanbu.[5]

Figure 2 shows the relative positions in parameter space of the regimes studied by previous authors for laminar flow as well as that studied in the present paper. First of all, we noticed that there are certain regimes that have not yet been investigated, for example, the transition region between the asymptotic solution studied by Benton and Boyer[4] and that studied by Berman and Mockros.[7] Second, we found that the detailed structure of the flow field has not yet been fully explored. Furthermore, it is also interesting to see how well the asymptotic solutions behave as certain parameters vary. Therefore, the goal of the present paper is to carry out a detailed numerical study of the full nonlinear equations, so that the detailed flow physics can be investigated for wide ranges of parameters. The ranges of parameters for the present study are indicated in Fig. 2. The present secondary flow problem is somewhat more interesting than the secondary flow in curved pipes in the sense that it is a two-parameter problem, and both of them may vary from very small to very large values. Although it is also a two-parameter problem for

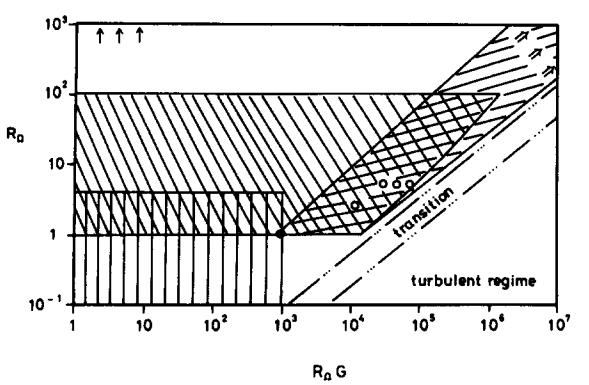

FIG. 2. Layout of the parameter space. ↑, asymptotic solution for $R_\Omega \gg 1$, $R_\Omega \gg R$ (Benton and Boyer); ⇑, asymptotic solution for $R_\Omega R \gg 1$, $R \gg R_\Omega$ (Ito and Nanbu); O, numerical solution by Duck; ||||, perturbation solution by Berman and Mockros; ////, the experimental study by Ito and Nanbu; and \\\\, the present calculation.

flow in a curved pipe in general, one of its governing parameters, the ratio of the pipe radius to the radius of curvature, is always restricted to be less than unity. The results of the present study also have engineering applications in the design of the cooling channels inside the rotating blades of gas turbines (see Morris[9]) and other pipe flow systems in a rotating frame.

II. FORMULATION

The governing equations for a steady incompressible Newtonian fully developed pipe flow with constant viscosity in the rotating coordinates (r',θ,z') shown in Fig. 1 are

$$\frac{\partial u'}{\partial r'} + \frac{u'}{r'} + \frac{1}{r'}\frac{\partial v'}{\partial \theta} = 0, \tag{1a}$$

$$u'\frac{\partial u'}{\partial r'} + \frac{v'}{r'}\frac{\partial v'}{\partial \theta} - \frac{v'^2}{r'} = -\frac{1}{\rho}\frac{\partial p^{*\prime}}{\partial r'} + 2\Omega w' \cos\theta + \nu\left(\nabla'^2 u' - \frac{u'}{r'^2} - \frac{2}{r'^2}\frac{\partial v'}{\partial \theta}\right), \tag{1b}$$

$$u'\frac{\partial v'}{\partial r'} + \frac{v'}{r'}\frac{\partial v'}{\partial \theta} + \frac{u'v'}{r'} = -\frac{1}{\rho r'}\frac{\partial p^{*\prime}}{\partial \theta} - 2\Omega w' \sin\theta + \nu\left(\nabla'^2 v' + \frac{2}{r'^2}\frac{\partial u'}{\partial \theta} - \frac{v'}{r'^2}\right), \tag{1c}$$

$$u'\frac{\partial w'}{\partial r'} + \frac{v'}{r'}\frac{\partial w'}{\partial \theta} = -\frac{1}{\rho}\frac{\partial p^{*\prime}}{\partial z'} - 2\Omega u' \cos\theta + 2\Omega v' \sin\theta + \nu\nabla'^2\omega', \tag{1d}$$

where $p^{*\prime} = p' - \frac{1}{2}\rho\Omega^2(x'^2 + z'^2)$ is the reduced pressure, which includes the centrifugal effect resulting from rotation and the operator

$$\nabla'^2 = \frac{\partial^2}{\partial r'^2} + \frac{1}{r'}\frac{\partial}{\partial r'} + \frac{1}{r'^2}\frac{\partial^2}{\partial \theta^2}.$$

The axial reduced pressure gradient $-\partial p^{*\prime}/\partial z' (\equiv G^*)$ is constant for fully developed flow. We now define a streamfunction ψ' such that

$$u' = \frac{1}{r'}\frac{\partial \psi'}{\partial \theta}, \quad v' = -\frac{\partial \psi'}{\partial r'}, \tag{2}$$

and thus the continuity equation (1a) is satisfied automatically. After a certain amount of routine manipulation of the equations of motion, the problem reduces to the solution of the following set of dimensionless equations:

$$\nabla^2\psi = -\zeta, \tag{3a}$$

$$\nabla^2\zeta + \frac{1}{r}\frac{\partial \psi}{\partial r}\frac{\partial \zeta}{\partial \theta} - \frac{1}{r}\frac{\partial \psi}{\partial \theta}\frac{\partial \zeta}{\partial r} = \frac{2}{r}\frac{\partial w}{\partial \theta}\cos\theta + 2\frac{\partial w}{\partial r}\sin\theta, \tag{3b}$$

$$\nabla^2 w + \frac{1}{r}\frac{\partial \psi}{\partial r}\frac{\partial w}{\partial \theta} - \frac{1}{r}\frac{\partial \psi}{\partial \theta}\frac{\partial w}{\partial r} + R_\Omega G = R_\Omega^2\left(\frac{2}{r}\frac{\partial \psi}{\partial \theta}\cos\theta + 2\frac{\partial \psi}{\partial r}\sin\theta\right), \tag{3c}$$

where the problem is normalized through

$$r=\frac{r'}{a},\quad \psi=\frac{\psi'}{\nu},\quad \zeta=\frac{\zeta' a^2}{\nu},$$
$$w=\frac{a^3\Omega}{\nu^2}w',\quad \nabla^2=a^2\nabla'^2, \tag{4}$$

ζ' is the vorticity, and

$$G=G^* a^3/\rho\nu^2,\quad R_\Omega=\Omega a^2/\nu \tag{5}$$

are the two dimensionless parameters governing the flow field. The boundary conditions to be satisfied by Eqs. (3a)–(3c) are

$$\psi(1,\theta)=\frac{\partial\psi}{\partial r}(1,\theta)=w(1,\theta)=0. \tag{6}$$

Once we obtain the axial velocity $w(r,\theta)$, we can evaluate the dimensionless mean velocity:

$$w_m=\frac{2}{\pi}\int_0^\pi\int_0^1 w(r,\theta;R_\Omega,G)r\,dr\,d\theta \tag{7}$$

and the Reynolds number based on the mean velocity:

$$R=w_m' a/\nu=w_m/R_\Omega. \tag{8}$$

Equation (8) provides a relationship among the parameters R, R_Ω, and G since w_m is a function of R_Ω and G according to Eq. (7). One of the major concerns for the engineers is the change of the friction factor (f) due to the rotating effect. According to the definition of Ito and Nanbu,[5]

$$f=G^*/\tfrac{1}{2}\rho w_m'^2(1/2a),$$

which may be written as

$$f=4(G/R^2), \tag{9a}$$

in terms of the present dimensionless parameters. The friction factor for a stationary fully developed pipe flow (Hagen–Poiseuille) is

$$f_s=32/R.$$

Hence

$$f/f_s=\tfrac{1}{8}G/R. \tag{9b}$$

III. NUMERICAL METHOD

The numerical method employed here is basically the same as that employed by Collins and Dennis[10] for solving the flow in curved pipes. It is an iteration method in which solutions are first obtained by the method of upwind difference and then corrected using the difference correction method of Fox[11] so that the final solutions are correct to central difference accuracy. The major differences between the present method and the method by Collins and Dennis are the iteration procedure and the criterion for convergence.

We employed the alternating direction iterative method (ADI) for iteration instead of the Gauss–Seidel procedure, which was employed by Collins and Dennis. The criterion for convergence according to Collins and Dennis[10] is

$$|\zeta^{(m+1)}(1,\theta)-\zeta^{(m)}(1,\theta)|<10^{-4} \tag{10}$$

for all the grids along the wall, where the superscript $(m+1)$ and (m) represent the $(m+1)$th and mth iterations, respectively. This criterion is not suitable for the present problem since ζ is not of order unity for all the cases studied here. Hence we employed the following criteria for convergence:

$$\frac{|w^{(m+1)}(r,\theta)-w^{(m)}(r,\theta)|}{|w^{(m+1)}(r,\theta)|}<10^{-4},$$
$$\frac{|\psi^{(m+1)}(r,\theta)-\psi^{(m)}(r,\theta)|}{|\psi^{(m+1)}(r,\theta)|}<10^{-4} \tag{11a}$$

for all the grids inside the calculating domain,

$$\frac{|\zeta^{(m+1)}(1,\theta)-\zeta^{(m)}(1,\theta)|}{|\zeta^{(m+1)}(1,\theta)|}<10^{-4} \tag{11b}$$

for all the grids along the wall, and

$$\frac{|D_0^{(m+1)}(r,\theta)-D_0^{(m)}(r,\theta)|}{|D_0^{(m+1)}(r,\theta)|}<10^{-4},$$
$$\frac{|E_0^{(m+1)}(r,\theta)-E_0^{(m)}(r,\theta)|}{|E_0^{(m+1)}(r,\theta)|}<10^{-4} \tag{11c}$$

for all the grids inside the domain, where D_0 and E_0 are the axial velocity and vorticity correction terms for obtaining a second-order accurate solution, respectively. Since the flow field is symmetric about $y=0$, according to Eqs. (3a)–(3c) and (6), we shall carry out the finite difference calculation for the semicircular region from $\theta=0$ to π. Solution procedures are similar to those in Collins and Dennis.[10] Details of the discretizations and finite difference equations for the present problem can be found from Hsu.[12]

IV. RESULTS AND DISCUSSIONS

Calculations were carried out for a large number of cases ranging from $R_\Omega=1$ to 100 and from $R_\Omega G=1$ to $O(10^4)$ or $O(10^6)$, depending on the magnitude of R_Ω. Some of the typical results are listed in Table I and plotted in Figs. 3 and 4. The grid spacings for the calculations are $\frac{1}{40}$ and $\pi/40$ in the r and θ directions, respectively. Table I summarizes the maximum values of w and ψ (denoted by $w_{\max}$ and $\psi_{\max}$) and their locations, the mean axial velocity w_m according to Eq. (7), the dimensionless parameters R_Ω^2, $R_\Omega G$, R, $K_I(=8R_\Omega R)$, and R_Ω/R, the friction factor ratio (f/f_s), and the friction factor ratio based on the experimental correlation by Ito and Nanbu[5] (f_I/f_s). Figures 3 and 4 show the contours for constant values of dimensionless axial velocity and secondary streamfunction with $w/w_{\max}$ (also $\psi/\psi_{\max}$) $=0$, 0.2, 0.4, 0.6, 0.8, and 0.95 (starting from zero at the wall $r=1$ and increasing their values away from the wall). Also shown in the figures are the locations of maximum values, which are denoted by closed circles. According to the experimental correlation by Ito and Nanbu, the critical Reynolds numbers (R_{cr}) for the present problem are 1250, 1466, and 2122 when $R_\Omega^2=100$, 400, and 10 000, respectively. No correlation is available when $R_\Omega<8$, but we may expect $R_{cr}\approx 1150$ according to the experimental result for the stability of Poiseuille flow. [Note that $R=w_m a/\nu$ in the present paper instead of $R=w_m(2a)/\nu$ employed by Ito and Nanbu.] No further cases have been simulated for $R_\Omega^2\leqslant 100$ with $R_\Omega G$ larger than those listed in Table I as a result of the stability consideration. For cases $R_\Omega^2=400$ (and 10^4) with $R_\Omega G$ greater than those values listed in Table I and cases with $R_\Omega^2>14\,400$, we have difficulty obtaining con-

TABLE I. Representative cases for the present study.

Case	R_Ω^2	$R_\Omega G$	w_{max}		ψ_{max}		w_m	R	K_I	R_Ω/R	f/f_s	f_I/f_s
1	1	1	0.249	(0.000, 0°)	0.001 48	(0.450, 90°)	0.125	0.125	0.996	8.03	1.004	
2	1	10	2.49	(0.000, 0°)	0.0148	(0.450, 90°)	1.25	1.25	9.96	0.803	1.004	
3	1	100	24.9	(0.025, 0°)	0.148	(0.450, 90°)	12.5	12.5	99.6	0.0803	1.004	
4	1	1 000	238	(0.250, 0°)	1.31	(0.450, 85.5°)	120	120	959	0.008 35	1.043	1.082
5	1	10 000	1 746	(0.525, 0°)	5.23	(0.525, 85.5°)	961	961	7 684	0.001 04	1.301	1.332
6	1	12 000	2 037	(0.550, 0°)	5.63	(0.550, 90°)	1 129	1129	9 032	0.000 886	1.329	1.360
7	6.25	6 250	1 172	(0.500, 0°)	4.21	(0.500, 85.5°)	632	253	5 053	0.009 89	1.237	1.266
8	25	10	2.31	(0.000, 0°)	0.0130	(0.450, 90°)	1.20	0.240	9.60	20.8	1.042	
9	25	25 000	3 788	(0.600, 0°)	7.27	(0.575, 94.5°)	2 149	430	17 194	0.0116	1.454	1.487
10	25	50 000	6 915	(0.625, 0°)	9.12	(0.625, 99°)	3 918	784	31 341	0.006 38	1.595	1.630
11	25	75 000	9 807	(0.650, 0°)	10.3	(0.650, 103.5°)	5 537	1107	44 295	0.004 52	1.693	1.724
12	64	10	2.09	(0.000, 0°)	0.0109	(0.475, 90°)	1.14	0.143	9.15	55.9	1.093	
13	100	1	0.195	(0.000, 0°)	0.000 946	(0.475, 90°)	0.111	0.0111	0.884	905	1.131	
14	100	10	1.95	(0.000, 0°)	0.009 46	(0.475, 90°)	1.11	0.111	8.84	90.5	1.131	
15	100	100	19.5	(0.025, 0°)	0.0945	(0.475, 90°)	11.1	1.11	88.4	9.05	1.131	
16	100	1 000	193	(0.175, 0°)	0.912	(0.475, 85.5°)	109	10.9	875	0.91	1.143	
17	100	10 000	1 654	(0.525, 0°)	4.77	(0.550, 85.5°)	943	94.3	7 546	0.106	1.325	1.329
18	100	50 000	6 833	(0.625, 0°)	8.95	(0.625, 99°)	3 898	390	31 184	0.0257	1.603	1.629
19	100	100 000	12 446	(0.675, 0°)	11.2	(0.650, 103.5°)	7 042	704	56 337	0.014	1.775	1.796
20	100	180 000	20 465	(0.700, 0°)	13.3	(0.675, 108°)	11 550	1155	92 397	0.008 66	1.948	1.959
21	225	10	1.67	(0.325, 90°)	0.006 56	(0.500, 90°)	1.017	0.0678	8.136	221	1.229	
22	225	10 000	1 550	(0.500, 0°)	4.24	(0.550, 85.5°)	922	61.5	7 377	0.244	1.356	1.325
23	400	10	1.52	(0.450, 90°)	0.004 64	(0.525, 90°)	0.948	0.0474	7.58	422	1.319	
24	400	100	15.2	(0.450, 90°)	0.0464	(0.525, 90°)	9.47	0.474	75.8	42.2	1.319	
25	400	1 000	152	(0.450, 85.5°)	0.462	(0.525, 90°)	94.6	4.73	757	4.23	1.321	
26	400	10 000	1 437	(0.500, 49.5°)	3.61	(0.575, 85.5°)	895	44.7	7 158	0.447	1.397	(1.32)
27	400	13 000	1 846	(0.500, 13.5°)	4.29	(0.575, 85.5°)	1 141	57.1	9 128	0.351	1.424	(1.362)
28	400	15 000	2 119	(0.500, 0°)	4.67	(0.575, 90°)	1 302	65.1	10 416	0.307	1.440	(1.386)
29	400	50 000	6 516	(0.625, 0°)	8.28	(0.625, 99°)	3 825	191	30 608	0.105	1.634	1.624
30	400	100 000	12 081	(0.675, 0°)	10.7	(0.650, 103.5°)	6 963	348	55 700	0.0575	1.795	1.792
31	400	180 000	20 071	(0.700, 0°)	12.9	(0.675, 108°)	11 467	573	91 736	0.0349	1.963	1.956
32	900	10 000	1 294	(0.550, 76.5°)	2.43	(0.600, 85.5°)	832	27.7	6 658	1.08	1.503	
33	1 600	10	1.21	(0.625, 90°)	0.001 67	(0.625, 90°)	0.777	0.0194	6.22	2 062	1.611	
34	1 600	10 000	1 193	(0.625, 85.5°)	1.63	(0.625, 85.5°)	772	19.4	6 218	2.06	1.608	
35	1 600	100 000	10 769	(0.650, 0°)	8.90	(0.675, 99°)	6 689	167	53 512	0.240	1.869	1.780
36	2 500	100 000	9 960	(0.600, 0°)	7.81	(0.700, 90°)	6 520	130	52 160	0.383	1.917	
37	3 600	100 000	9 197	(0.675, 63°)	6.70	(0.700, 90°)	6 342	106	50 736	0.568	1.971	
38	4 900	100 000	8 962	(0.725, 81°)	5.66	(0.725, 85.5°)	6 157	88.0	49 258	0.796	2.030	
39	10 000	10	0.846	(0.775, 90°)	0.000 345	(0.750, 90°)	0.567	0.005 67	4.54	17 637	2.204	
40	10 000	100	8.46	(0.775, 90°)	0.003 45	(0.750, 90°)	5.67	0.0567	45.4	1 764	2.204	
41	10 000	1 000	84.6	(0.775, 90°)	0.0345	(0.750, 90°)	56.7	0.567	454	176	2.204	
42	10 000	10 000	845	(0.775, 90°)	0.345	(0.750, 90°)	567	5.67	4 536	17.6	2.204	
43	10 000	100 000	8 237	(0.775, 85.5°)	3.36	(0.750, 81°)	5 595	56.0	44 760	1.79	2.234	
44	10 000	300 000	22 266	(0.750, 67.5°)	8.53	(0.750, 81°)	15 769	158	126 152	0.634	2.378	
45	10 000	400 000	29 050	(0.650, 0°)	10.3	(0.775, 81°)	20 443	204	163 544	0.489	2.446	
46	10 000	1 000 000	71 557	(0.750, 0°)	16.0	(0.800, 85.5°)	45 697	457	365 576	0.219	2.735	2.550
47	10 000	1 300 000	91 415	(0.775, 0°)	17.8	(0.800, 90°)	57 245	572	475 960	0.175	2.839	2.690

vergent solutions based on the present numerical method. Further illustrations and detailed discussions will be presented later in this section.

A. Grid dependence

Before we get into the details of the discussion, we first check the grid dependence. In the present calculations, four pairs of grid sizes have been used, namely,

$$h = \tfrac{1}{20},\quad k = \pi/20 \quad (21\times 21 \text{ grids}),$$
$$h = \tfrac{1}{30},\quad k = \pi/30 \quad (31\times 31 \text{ grids}),$$
$$h = \tfrac{1}{40},\quad k = \pi/40 \quad (41\times 41 \text{ grids}),$$
$$h = \tfrac{1}{50},\quad k = \pi/50 \quad (51\times 51 \text{ grids}).$$

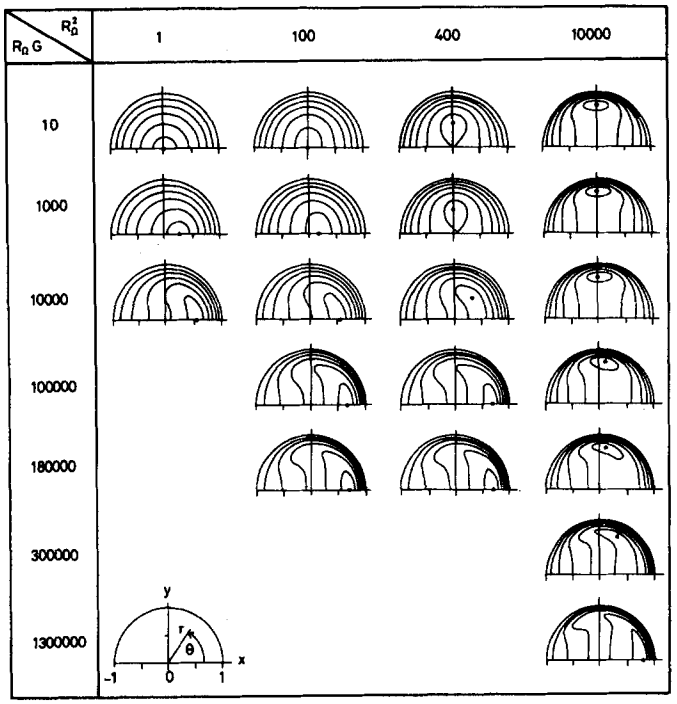

FIG. 3. Contours for constant axial velocity with values $w/w_{max} = 0$, 0.2, 0.4, 0.6, 0.8, and 0.95 (starting from zero at the wall $x^2 + y^2 = 1$ and increasing their values away from the wall). The locations of w_{max} are denoted by closed circles. The figure in the lower left corner shows the coordinate system.

The results for eight cases using these four grid sizes are shown in Table II. Three representative properties, namely, w_{max}, ψ_{max}, and w_m, as well as the CPU time, are listed in the table for comparison. The calculations were carried out on the CONVEX C-1 computer without vectorization. The initial guesses of the field for w, ψ, and ζ were all set to zero. The general trend of these results as the grid sizes are decreased tends to indicate the solutions for the case of (41×41) grids are probably accurate to within 1% tolerance up to $R_\Omega = 100$ and $R_\Omega G = 10^5$. We also checked the detailed variations of the flow field for different grid spacing, and found that $h = \frac{1}{40}$ and $k = \pi/40$ is indeed a reasonably accurate choice for grid spacing. It is worth it here to point out that the CPU time increases rapidly as the grid spacing decreases. In order to obtain a compromise between the cost of the computer time and the accuracy of the solution, we carried out all the numerical simulations with $h = \frac{1}{40}$ and $k = \pi/40$ in this paper.

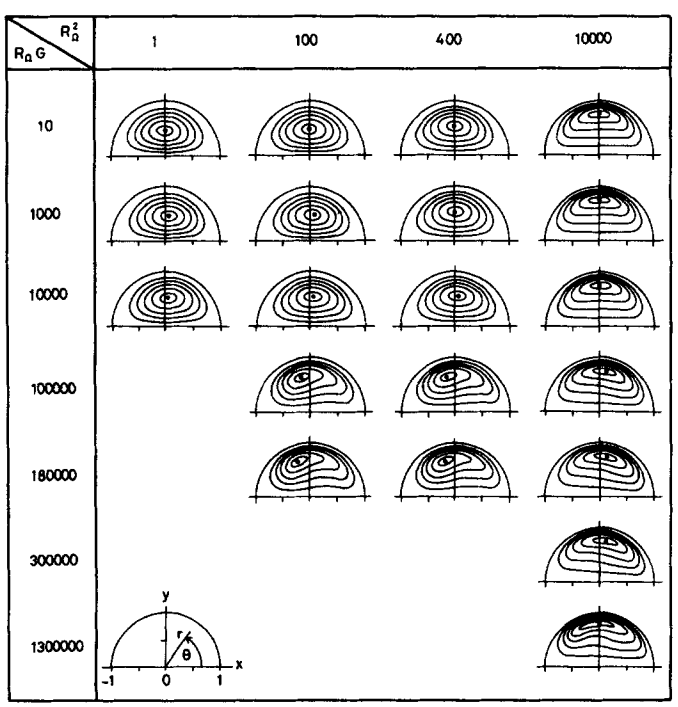

FIG. 4. Contours for the constant secondary streamfunction with values $\psi/\psi_{max} = 0$, 0.2, 0.4, 0.6, 0.8, and 0.95. The representing convention is the same as that in Fig. 3.

B. Validity of the computer program

First we check the present numerical solution against the asymptotic solution by Berman and Mockros[7] for small values of N_α ($= R_\Omega/48$). Figure 5 shows the contours for constant ψ and w with their values ψ/ψ_{max} (and w/w_{max}) = 0, 0.125, 0.25, 0.375, 0.5, 0.625, 0.75, and 0.875 (starting from zero at the wall at $r = 1$ and increasing their values away from the wall). The agreement between the present calculation and the asymptotic solution is excellent, at least for this set of parameters, i.e., $R_\Omega = 1$ and $R_\Omega G = 10$. Further comparison will be shown later in Fig. 13(b).

Next we check the present calculations with the experimental results by Ito and Nanbu via the friction factor ratio. Ito and Nanbu[5] proposed the following correlation according to their experimental findings:

$$f_t/f_s = 0.0883K_l^{1/4}(1 + 11.2K_l^{-0.325}) \tag{12a}$$

for

$$2.2\times10^2 < K_l < 10^7, \quad R_\Omega/R < 0.25, \tag{12b}$$

where

$$K_l = 8R_\Omega R. \tag{12c}$$

Table I lists our numerical calculations according to Eq. (9b) together with the correlation from Eq. (12a). We found that the present calculations agree well with the experimental correlations, including cases like $R_\Omega = 100$ and $R_\Omega G = 10^6$ in which the grid dependence has not yet been checked. The numbers within parentheses shown in the last column of Table I are some cases outside the parameter ranges for the experimental correlation according to Eq. (12b); they still agree well with the present calculations.

Third, we check the asymptotic behavior for $R_\Omega \gg R$ and $R_\Omega \gg 1$ of the present calculation with the asymptotic solution by Benton and Boyer.[4] Benton and Boyer proposed that (1) the viscous effects are important only in the thin boundary layer along the wall; (2) the flow in the core is geostrophic, which implies that $w = w(x)$ and $\psi = \psi(y)$, where $x = x'/a$ and $y = y'/a$; and (3) the inertia effects may be neglected everywhere. We shall check these three points according to our results shown in Table I and Figs. 3 and 4. For cases $R_\Omega = 100$ and $R_\Omega G = 10$–10^4 (i.e., $R_\Omega/R = 17.64$–$17\,637$), we found that most of the deformation indeed occurs next to the wall, except the region in the vicini-

TABLE II. Variations of w_m, w_{max}, ψ_{max}, and CPU time in seconds with different grids.

R_Ω^2	$R_\Omega G$	*Grids*	w_m	w_{max}	ψ_{max}	CPU (sec)
1^2	10	21×21	1.24	2.49	0.015 0	105.3
		31×31	1.25	2.49	0.014 8	415.5
		41×41	1.25	2.49	0.014 8	1 132.7
1^2	10^4	21×21	955	1 743	5.26	82.2
		31×31	959	1 746	5.24	369.3
		41×41	961	1 746	5.23	958.0
		51×51	961	1 747	5.23	2 390.7
10^2	10^3	21×21	109	193	0.913	96.6
		31×31	109	193	0.912	422.7
		41×41	109	193	0.912	1 517.1
		51×51	109	193	0.911	2 663.3
10^2	10^4	21×21	937	1 646	4.80	86.4
		31×31	942	1 652	4.78	357.2
		41×41	943	1 654	4.77	1 071.3
		51×51	944	1 654	4.77	2 537.5
10^2	10^5	21×21	6943	12 353	11.3	175.6
		31×31	7016	12 421	11.2	1 141.1
		41×41	7042	12 446	11.2	4 172.1
		51×51	7054	12 454	11.1	9 682.5
100^2	10	21×21	0.542	0.809	0.000 352	155.6
		31×31	0.560	0.838	0.000 346	1 150
		41×41	0.567	0.846	0.000 345	4 959.8
		51×51	0.570	0.850	0.000 344	13 175.8
100^2	10^4	21×21	542	809	0.352	169.5
		31×31	560	836	0.346	1 157.9
		41×41	567	845	0.345	4 810.4
		51×51	570	850	0.344	14 993.0
100^2	10^5	31×31	5528	8 153	3.37	1 448.4
		41×41	5595	8 237	3.36	5 430.1
		51×51	5627	8 280	3.35	15 831.6

ty of $\theta = 0$ and π, where the Coriolis effect is minimized. This implies that a boundary layer region is formed next to the wall. The axial velocity and the streamfunction contours for the above cases shown in Figs. 3 and 4 also indicate that the flow field in the core region is geostrophic. To quantify this point, we have the axial velocity on the symmetric plane as

$$w/w_{max} = (1 - x^2)^{3/4} \tag{13a}$$

and the streamfunction along the y axis as

$$\psi/\psi_{max} = (R_\Omega G/2R_\Omega^2 \psi_{max})y, \tag{13b}$$

according to Ito and Nanbu[5] (or Benton and Boyer[4]) in terms of the present parameters and variables inside the core. Figure 6(a) shows Eq. (13a) together with the present numerical solutions for $R_\Omega = 100$ and $R_\Omega G = 10$–10^4. We found the numerical solution agrees with the asymptotic solution. Figure 6(b) compares Eq. (13b) with the numerical results for $R_\Omega = 100$ and $R_\Omega G$ 10–10^4. We found that the agreement is fair up to the location where ψ_{max} occurs. Here, it is worth mentioning that the term $R_\Omega G/(2R_\Omega^2 \psi_{max}) \approx 1.45$ in Eq. (13b) and the numerical results in Figs. 6(a) and 6(b) are almost independent of $R_\Omega G$ for $R_\Omega G = 10$–10^4, so that the data collapse onto a single curve for these cases as shown in the figures. Finally, for $R_\Omega \gg R$ and $R_\Omega \gg 1$, the inertia term can be set to zero so that Eqs. (3a)–(3c) are reduced to a set of linear equations. Such linear equations together with the boundary conditions [Eq. (6)] indicate that

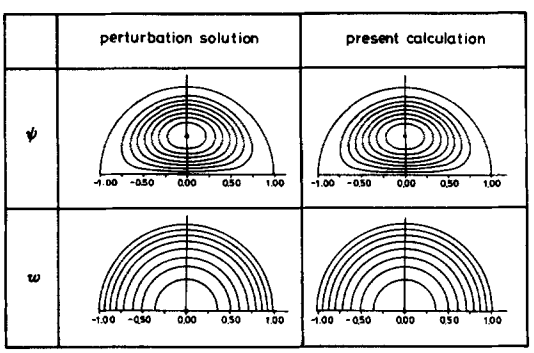

FIG. 5. Comparison between the perturbation solution (Berman and Mockros) and the present calculation for $R_\Omega = 1$ and $R_\Omega G = 10$. The contour values for w/w_{max} (and ψ/ψ_{max}) are 0, 0.125, 0.25, 0.375, 0.5, 0.625, 0.75, and 0.875. The representing convention is the same as that in Fig. 3.

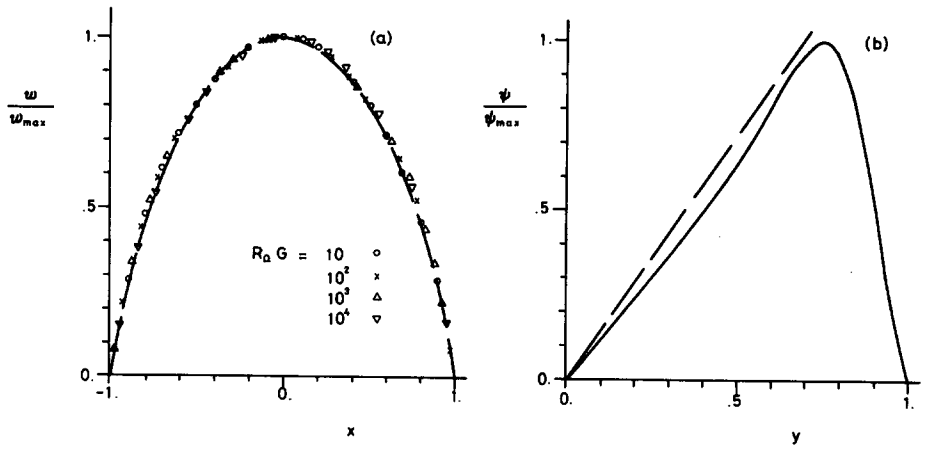

FIG. 6. A comparison between the asymptotic solution by Benton and Boyer for $R_\Omega \gg 1$, $R_\Omega \gg R$ (dashed line), and the present calculation for $R_\Omega = 100$, $R_\Omega G = 10$–10^4 (○, ×, △, ▽, solid line): (a) the axial velocity profile on the symmetric plane; and (b) the secondary streamfunction along the y axis.

$$w(r,\theta) = w(r,\pi-\theta), \quad \psi(r,\theta) = \psi(r,\pi-\theta), \quad \zeta(r,\theta) = \zeta(r,\pi-\theta). \tag{14}$$

The cases for $R_\Omega = 100$ and $R_\Omega G = 10$–10^4 shown in the last column of Figs. 3 and 4 indeed show that both the w and ψ contours are symmetric about the y axis.

C. The general flow structure

Now, we have a certain confidence to carry out detailed numerical simulations. Since this is a two-parameter problem, a large number of cases are required to give a clear picture of the flow structure. We have run many cases and the most representative cases among them have already been shown in Figs. 3 and 4 and Table I. Here we shall give a detailed discussion on these results.

We found that there are four types of flow regimes for the present problem, namely, regime A, B, C, and D, according to the results shown in Figs. 3 and 4 and Table I. The ranges of parameters for these flow regimes are sketched qualitatively in Fig. 7 together with those studied by Berman and Mockros. The edges of these regimes are determined approximately by the scaling analyses together with the present numerical results, which will be discussed later in this section. We found that the perturbation solution by Berman and Mockros covers the entire regime A and part of the regimes B, C, and D. Hence the present solution may be regarded as an extension of the perturbation solution. The flow field for all these regimes is symmetric about the x-z plane, which is thus called the symmetric plane. The general trend for the present results shows that the strength of the main stream and that of the secondary flow increase with $R_\Omega G$ for fixed values of R_Ω^2, but decrease as R_Ω^2 increases for fixed values of $R_\Omega G$. Different regimes are characterized by different shapes of the axial velocity profiles, which were predicted qualitatively by Berman and Mockros.[7]

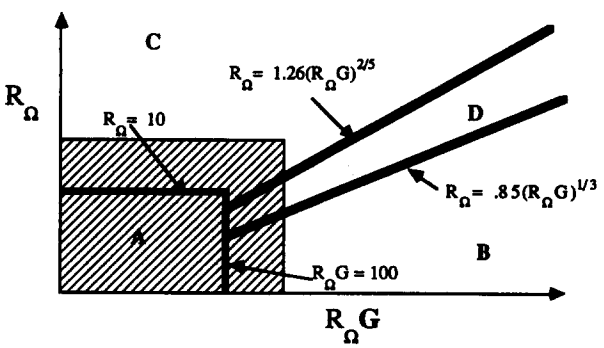

FIG. 7. Sketch of the relative positions in the parameter space for the four flow regimes. Different regimes are separated by solid bold lines. Region in shaded area is the approximate region covered by the perturbation solution of Berman and Mockros.

(1) *Regime A:* When both $R_\Omega G$ and R_Ω^2 are sufficiently small ($R_\Omega \leqslant 10$ and $R_\Omega G \leqslant 100$), the secondary flow is too weak to modify the main flow effectively, such that the axial velocity profile is essentially axisymmetric and parabolic with the maximum value occurring at or very close to the center of the pipe. Cases with this kind of flow pattern belong to regime A. Typical examples are cases 1–3,8, and 12–15 in Table I, with the corresponding flow patterns shown in Figs. 3 and 4. Both the magnitudes of the axial velocity and the secondary flow of this regime increase linearly with $R_\Omega G$ for fixed values of R_Ω^2, but decrease slightly as R_Ω^2 increases for fixed values of $R_\Omega G$. The location of ψ_{max} occurs on $\theta = 90°$, and is shifted slightly outward as R_Ω^2 increases for fixed values of $R_\Omega G$, but stays at the same position as $R_\Omega G$ varies for fixed values of R_Ω^2. The asymptotic solutions by Baura,[2] Benton,[3] and Berman and Mockros[7] include this regime.

(2) *Regime B:* When R_Ω is small but $R_\Omega G$ is large [$R_\Omega < 0.85(R_\Omega G)^{1/3}$ and $R_\Omega G > 100$], the location of w_{max} is shifted outward along $\theta = 0°$ so that the axial velocity profile is skewed toward the pressure side (positive x). Cases with such a flow pattern belong to regime B. Examples for this regime are cases 4–7, 9–11, 16–20, 22, 28–31, 35–36, and 45–47 in Table I. The flow patterns in this regime are similar to those in curved pipes in the loosely coiled pipe limit as

expected from the governing equations. For small values of R_Ω^2, the terms on the right-hand side of Eq. (3c) can be set to zero, and Eqs. (3a)–(3c) then become a similar equation set to that in Dennis and Collins for flow in curved pipes. The Coriolis force in the present regime plays the similar role as the centrifugal force in curved pipe flow and pushes the location of $w_{\max}$ outward along the symmetric plane via the secondary flow.

(3) *Regime C:* When $R_\Omega G$ is small but R_Ω is large [$R_\Omega \geqslant 1.26(R_\Omega G)^{2/5}$ and $R_\Omega > 10$], the rotation effect dimples the axial velocity profile at the center and creates a dumbell-like profile with two maxima, one along $\theta = 90°$ and one along $\theta = 270°$. Cases with this kind of flow pattern belong to regime C. Cases 21, 23–24, 33, and 39–42 in Table I are typical examples for this regime. The locations of $w_{\max}$ and $\psi_{\max}$ do not depend on $R_\Omega G$ but move continuously outward along $\theta = 90°$ (and 270°) as R_Ω increases. Both the strength of the axial velocity and the secondary flow increase linearly with $R_\Omega G$ for fixed R_Ω, but decrease as R_Ω increases for fixed $R_\Omega G$.

(4) *Regime D:* It is the transition regime between regime B and C that occurs approximately when $0.85(R_\Omega G)^{1/3} \leqslant R_\Omega \leqslant 1.26(R_\Omega G)^{2/5}$ and $R_\Omega G > 100$. It is characterized by a skewed axial velocity profile with two maxima; one occurs at (r_1, θ_1) and the other occurs at $(r_1, 2\pi - \theta_1)$, where $0 < r_1 < 1$ and $0 < \theta_1 < 90°$. Examples are cases 25–27, 32, 34, 37–38, 43, and 44 in Table I. Typical flow patterns are shown in Fig. 3 for the cases $R_\Omega G = 10^4$, $R_\Omega^2 = 400$ and $R_\Omega G = 3 \times 10^5$, $R_\Omega^2 = 10^4$. Data shown in Table I indicate that regime D is quite a narrow region in the logarithmic plot of the parameter space (see Fig. 7). For example, regime D occurs approximately from $R_\Omega G = 10^3$ to 1.5×10^4 for $R_\Omega^2 = 400$ (cases 25–28) and from $R_\Omega = 15$–40 for $R_\Omega G = 10^4$ (cases 22, 26, 32, and 34) according to the data shown in Table I. It is also worth mentioning here that the flow pattern in regime D occurs when $R_\Omega / R = O(1)$ according to Table I.

The reason that we have different axial velocity profiles for different regimes can be understood through the force balance in the governing equations. It is the secondary flow that makes the axial velocity profile different from the parabolic profile in Poiseuille flow. The effect of the secondary flow enters the governing equation for w [Eq. (3c)] through two terms: the convection term and the Coriolis term. In the absence of these two terms, Eq. (3c) leads to the Poiseuille solution which has an axisymmetric and parabolic profile. The relative importance among the four terms in Eq. (3c) depends on the magnitudes of $R_\Omega G$ and R_Ω^2, and shows different flow patterns for different regimes. The axial pressure gradient is the driving term and hence is always important. The viscous term is always important next to the wall, but may not be significant in the core region for certain ranges of parameters. The scales in Eq. (4) are convenient for the present calculation, but not suitable for illustrating the force mechanisms. In order to study the force balance for various regimes, we had to rescale the problem through the following simple scaling analyses.

When both R and R_Ω are small, the viscous term is important and is of the same order as the driving term G^*/ρ in Eq. (1d) throughout the whole flow field; the Coriolis force, the viscous force, and the pressure term in Eqs. (1b) and (1c) are of the same order; and Eq. (1a) shows that $u' \sim v'$. A simple scaling analysis based on these arguments shows that the proper scales for w' and ψ' are $(\nu/a)G$ and $\nu R_\Omega G$, respectively. Equation (3c) then becomes

$$\nabla^2 \hat{w} + R_\Omega G\left(\frac{1}{r}\frac{\partial \hat{\psi}}{\partial r}\frac{\partial \hat{w}}{\partial \theta} - \frac{1}{r}\frac{\partial \hat{\psi}}{\partial \theta}\frac{\partial \hat{w}}{\partial r}\right) + 1 = R_\Omega^2\left(\frac{2}{r}\frac{\partial \hat{\psi}}{\partial \theta}\cos\theta + 2\frac{\partial \hat{\psi}}{\partial r}\sin\theta\right) \tag{15a}$$

if it is rescaled through

$$\hat{w} = w/R_\Omega G, \quad \hat{\psi} = \psi/R_\Omega G. \tag{15b}$$

The data shown in Table I (cases 1–3, 8, and 12–15) indicate that $\hat{w} = O(1)$ and $\hat{\psi} = O(10^{-3})$ for $R_\Omega \leqslant 10$ and $R_\Omega G \leqslant 100$. Both the convection term and the Coriolis term are then of one order less than the viscous term or pressure term in Eq. (15a) when $R_\Omega \leqslant 10$ and $R_\Omega G \leqslant 100$. Hence we have essentially axisymmetric profiles for the axial velocity when both $R_\Omega G$ and R_Ω^2 are small (i.e., regime A).

As $R_\Omega G$ increases by keeping R_Ω small and fixed, the convection term in Eq. (15a) increases. The secondary flow across the r-θ plane also increases as $R_\Omega G$ increases. Such cross-flow shifts the location of the maximum axial velocity outward along $\theta = 0$ in the manner similar to the flow in curved pipes. When $R_\Omega G$ is sufficiently large, the scales in Eq. (15b) become invalid. In such a case, the convection term balances the driving term G^*/ρ in Eq. (1d) in the core region; the Coriolis term, the pressure term, and the convection term are of the same order in Eqs. (1b) and (1c); and the continuity shows $u' \sim v'$. Based on these arguments, scaling analysis shows that the proper scales for w' and ψ' are $[\nu^2/(a^3\Omega)](R_\Omega G)^{2/3}$ and $\nu(R_\Omega G)^{1/3}$. Equation (3c) then is rescaled as

$$\frac{1}{(R_\Omega G)^{1/3}}\nabla^2 \tilde{w} + \frac{1}{r}\frac{\partial \tilde{\psi}}{\partial r}\frac{\partial \tilde{w}}{\partial \theta} - \frac{1}{r}\frac{\partial \tilde{\psi}}{\partial \theta}\frac{\partial \tilde{w}}{\partial r} + 1 = \frac{R_\Omega^2}{(R_\Omega G)^{2/3}}\left(\frac{2}{r}\frac{\partial \tilde{\psi}}{\partial \theta}\cos\theta + 2\frac{\partial \tilde{\psi}}{\partial r}\sin\theta\right), \tag{16a}$$

where

$$\tilde{w} = w/(R_\Omega G)^{2/3}, \quad \tilde{\psi} = \psi/(R_\Omega G)^{1/3}. \tag{16b}$$

The data shown in Table I (cases 5–6, 9–11, 18–20, 29–31, 35, 46, and 47) indicate that the convection term is indeed of order unity and $\tilde{\psi} \approx O(10^{-1})$. The Coriolis term in Eq. (16a) is then of one order less than the convection term and plays only a minor role in affecting the shape of the axial velocity profile when $R_\Omega^2 \leqslant (R_\Omega G)^{2/3}$ for large values of $R_\Omega G$. The convection effect pushes the location of $w_{\max}$ along $\theta = 0$ and hence the axial velocity profile is skewed toward the pressure side in regime B. It is found from the data in Table I that this criterion also works for cases when $R_\Omega G$ is not so large. Detailed numerical data (from Table I and other simulations not shown here) indicate that we have the flow pattern of regime B when $R_\Omega G > 100$ and $R_\Omega < 0.85(R_\Omega G)^{1/3}$.

When R is small and R_Ω is large enough, Benton and Boyer[4] showed that the inertia term is negligible everywhere,

the core flow is geostrophic and the viscous effects are confined inside a boundary layer next to the wall. Hence we have the scale for ψ' as $\nu(R_\Omega G)R_\Omega^{-2}$ and v' (or u') as $(\nu/a)(R_\Omega G)R_\Omega^{-2}$ in the core region by balancing the Coriolis force to the driving term G^*/ρ in Eq. (1d). Let v'' and w'' be the scales for v' and w' inside the boundary layer, and δ be the scale for the boundary layer thickness. Conservation of mass for the secondary flow in the r'-θ plane requires that $v''\delta \sim v'a \sim \psi'$. On balancing the Coriolis and viscous terms inside the boundary layer, we have $\nu v''/\delta^2 \sim \Omega w''$ and $\nu w''/\delta^2 \sim \Omega v''$. Therefore we may solve for v'', w'', and δ based on the above relations. The results are $\delta/a \sim R_\Omega^{-1/2}$, $v'' \sim (\nu/a)(R_\Omega G)R_\Omega^{-3/2}$, and $w'' \sim (\nu^2/a^3\Omega)(R_\Omega G) \times R_\Omega^{-1/2}$, which agree with the integral analysis by Ito and Nanbu.[5] The scale for w' inside the core is the same as that inside the boundary layer, i.e., $w' \sim w''$. Hence Eq. (3c) can be rescaled as

$$R_\Omega^{-1/2}\nabla^2\bar{w} + \frac{R_\Omega G}{R_\Omega^{5/2}}\left(\frac{1}{r}\frac{\partial\bar{\psi}}{\partial r}\frac{\partial\bar{w}}{\partial\theta} - \frac{1}{r}\frac{\partial\bar{\psi}}{\partial\theta}\frac{\partial\bar{w}}{\partial r}\right) + 1 = \frac{2}{r}\frac{\partial\bar{\psi}}{\partial\theta}\cos\theta + 2\frac{\partial\bar{\psi}}{\partial r}\sin\theta \tag{17a}$$

for flow in the core, where

$$\bar{\psi} = \psi R_\Omega^{2}/R_\Omega G, \quad \bar{w} = wR_\Omega^{1/2}/R_\Omega G. \tag{17b}$$

When $(R_\Omega G)R_\Omega^{-5/2} \leqslant O(10^{-1})$, the convection term is of one order less than the Coriolis term, so that the shape of the axial velocity profile is mainly affected by the Coriolis force. The Coriolis term in Eq. (17a) is maximized when $\bar{v} = \partial\bar{\psi}/\partial r$ is maximized and $\theta = 90°$. As stated in the previous scaling, the velocity of the secondary flow inside the boundary layer is of order $R_\Omega^{1/2}$ greater than that in the core. The maximum value of $\bar{v}$ then occurs somewhere near the outer edge of the boundary layer at $\theta = 90°$, which implies that the Coriolis force is also maximized there. Also note that $\bar{v}$ is positive there so that the Coriolis force enhances the axial velocity at the outer edge of the boundary layer. On the other hand, $\bar{v}$ is negative in the core and is of order $R_\Omega^{1/2}$ less than its maximum value. The Coriolis force then retards the axial velocity in the core by a small amount in comparing with the enhancement at the outer edge of the boundary layer. Hence we may have the dumbell-like two-maxima profile in regime C according to Eq. (17a) when R_Ω is large enough and R (proportional to G) is sufficiently small. Detailed numerical data according to Table I and other simulations (not shown here) indicate that we have the flow pattern of regime C when $R_\Omega > 10$ and $R_\Omega > 1.26(R_\Omega G)^{2/5}$.

Now, we know that there are two mechanisms that may affect the shape of the axial velocity profile. Consider the right semicircular region in Fig. 1, the convection term shifts the location of w_{max} toward the wall along $\theta = 0°$ while the Coriolis force shifts it toward the wall along $\theta = 90°$. We have just studied cases when either of these two mechanisms, or both of them, are negligible. In case both of these two mechanisms are important and are not negligible in comparing with the driving term G^*/ρ, the location of w_{max} is shifted to a new position in the first quadrant of Fig. 1, so that the axial velocity profile is skewed with two maxima which was classified as the profile of regime D. This occurs when $0.85(R_\Omega G)^{1/3} \leqslant R_\Omega \leqslant 1.26(R_\Omega G)^{2/5}$ and $R_\Omega G \geqslant 100$ according to the above analyses and the numerical data in Table I.

In order to quantify the above scaling analyses, we calculate the terms in Eq. (3c) based on the present numerical solutions. First Eq. (3c) is multiplied by r, then integrated from $r = 0$ to r_c and from $\theta = 0$ to π, where $0 \leqslant r_c \leqslant 1$. After certain manipulation, we have

$$\frac{2}{\pi r_c^2 R_\Omega G}\left[-\int_0^\pi\int_0^{r_c} r\nabla^2 w\, dr\, d\theta - \int_0^\pi\int_0^{r_c}\left(\frac{\partial\psi}{\partial r}\frac{\partial w}{\partial\theta} - \frac{\partial\psi}{\partial\theta}\frac{\partial w}{\partial r}\right) dr\, d\theta + R_\Omega^2\int_0^\pi\int_0^{r_c}\left(\frac{2}{r}\frac{\partial\psi}{\partial\theta}\cos\theta + 2\frac{\partial\psi}{\partial r}\sin\theta\right) r\, dr\, d\theta\right] = 1. \tag{18}$$

The terms on the left-hand side are the viscous, convection, and Coriolis terms, respectively, normalized through the axial pressure gradient term. Table III shows the magnitudes of these terms in the core region for several typical cases when $r_c = 0.7125$. Note that the sum of these three terms should equal unity for a given case. The results shown in the table show some discrepancies as a result of the numerical approximations in evaluating these terms. The result for case 3 which belongs to regime A indeed shows that the viscous term dominates. As $R_\Omega G$ increases by holding R_Ω fixed, the convection term increases (see cases 4 and 5) and modifies the flow field. In case 5, the convection term is of the same order as the viscous term. Similar transitions from regime A to B can also be observed from cases 14, 16, and 19 in Table III for larger values of R_Ω. In case 19, $R_\Omega G$ is large enough that the convection term dominates and balances the axial pressure gradient term as expected from Eq. (16a). When R_Ω is sufficiently large, say, $R_\Omega = 100$, cases 39, 41, and 43 in Table III show that the Coriolis term dominates and is of one order greater than the viscous term. It balances the axial pressure gradient term and thus confirms the geostrophic flow pattern in the core region proposed by Benton and Boyer.[4] Recall that the scaling analysis leading to Eqs. (17a) and (17b) is based on the argument of Benton and Boyer. In order to study the force mechanisms next to the wall, we also calculated the viscous term, the convection term, and the Coriolis term in Eq. (18) with $r_c = 0.9875$ for cases 39, 41, and 43, and found that they are equal to 0.984, 0.8×10^{-22}, and 0.34×10^{-1} for case 39; 0.984, 0.14×10^{-6}, and 0.34×10^{-1} for case 41; and 0.981, 0.13×10^{-2}, and 0.34×10^{-1} for case 43. By comparing these results with the corresponding results in Table III, we indeed found that the viscous effect is confined inside a thin boundary layer next to the wall, and that the convection term is negligible everywhere in the flow field, as proposed by Benton and Boyer before. Cases 26 and 44 show that both the convection term and the Coriolis term are of the same order and hence they belong to regime D. Cases 23, 25, 26, and 30 (also 39, 41, 43, 44, and 47) show the changes of the relative importance of each term as the flow transmits from regime C to D and then to B. The results agree with the above scaling analyses.

The flow pattern transmits from one regime to another smoothly as the parameters vary. First consider the transi-

TABLE III. The relative importance of the various forces in the core region (from $r = 0$ to 0.7125).

Case	R_Ω^2	$R_\Omega G$	Viscous term	Convection term	Coriolis term	Regime
3	1	100	0.998	0.55×10^{-3}	0.27×10^{-2}	A
4	1	1 000	0.947	0.42×10^{-1}	0.24×10^{-2}	B
5	1	10 000	0.636	0.362	0.11×10^{-2}	B
14	100	10	0.829	0.31×10^{-6}	0.181	A
16	100	1 000	0.836	0.14×10^{-1}	0.176	B
19	100	100 000	0.191	0.803	0.29×10^{-1}	B
23	400	10	0.631	0.2×10^{-6}	0.398	C
25	400	1 000	0.637	0.22×10^{-2}	0.397	C
26	400	10 000	0.553	0.137	0.326	D
30	400	100 000	0.183	0.726	0.112	B
39	10 000	10	0.100	0.13×10^{-8}	0.923	C
41	10 000	1 000	0.101	0.36×10^{-5}	0.923	C
43	10 000	100 000	0.85×10^{-1}	0.35×10^{-1}	0.903	C
44	10 000	300 000	0.22×10^{-1}	0.238	0.766	D
47	10 000	1 300 000	0.42×10^{-1}	0.702	0.366	B

$$\text{Viscous term} = -\frac{2}{\pi r_c^2 R_\Omega G}\int_0^{\pi}\int_0^{r_c} r\nabla^2 w\, dr\, d\theta$$

$$\text{Convection term} = -\frac{2}{\pi r_c^2 R_\Omega G}\int_0^{\pi}\int_0^{r_c}\left(\frac{\partial\psi}{\partial r}\frac{\partial w}{\partial\theta}-\frac{\partial\psi}{\partial\theta}\frac{\partial w}{\partial r}\right)dr\, d\theta$$

$$\text{Coriolis term} = \frac{2R_\Omega^2}{\pi r_c^2 R_\Omega G}\int_0^{\pi}\int_0^{r_c}\left(\frac{2}{r}\frac{\partial\psi}{\partial\theta}\cos\theta + 2\frac{\partial\psi}{\partial r}\sin\theta\right) r\, dr\, d\theta$$

tion from regime A to B. For a given small value of R_Ω, the location of w_{max} is shifted continuously outward along $\theta = 0$ as $R_\Omega G$ increases, as shown by the figures in the first two columns of the diagrams of Fig. 3 and the values listed in Table I for $R_\Omega^2 = 1$ and 100. The location of ψ_{max} is first shifted a little bit to the right from $\theta = 90°$ as $R_\Omega G$ increases, which agrees with the analysis by Berman and Mockros, and then is shifted to the left as $R_\Omega G$ increases further for a given value of R_Ω. The secondary streamfunction is distorted even more as $R_\Omega G$ increases. Table I also lists the values of the dimensionless parameters $K_l (= 8R_\Omega R)$ and R_Ω/R, which were employed by Ito and Nanbu. We found that the flow field approaches the limiting case $R \gg R_\Omega$, $R_\Omega R \gg 1$ studied by Ito and Nanbu[5] as K_l increases with small values of R_Ω/R (see the last figure in each column of Figs. 3 and 4). Figure 8(a) shows the axial velocity profile along the symmetric plane for $R_\Omega = 10$ as $R_\Omega G$ varies. The flow pattern is skewed continuously from the parabolized profile (Hagen–Poiseuille) as the effect of rotation increases. Figure 8(b) shows the variation of w along the y axis with $R_\Omega G$ for $R_\Omega = 10$. The transition from regime A to C can be seen clearly if we go through the figures on the first row of diagrams of Figs. 3 and 4. The location of w_{max} is shifted outward along the y axis and the flow tends to approach the geostrophic core pattern [i.e., $w = w(x)$, $\psi = \psi(y)$] as R_Ω increases. To give a further illustration, we plot the velocity profiles along the y axis for $R_\Omega G = 10$: $R_\Omega = 1$, 10, 20, 40, and 100 in Fig. 9. Note that the profile for $R_\Omega = 100$ indeed shows a flat region, i.e., $w \neq w(y)$, which is regarded as a feature of the geostrophic core for the limiting case $R_\Omega \gg 1$,

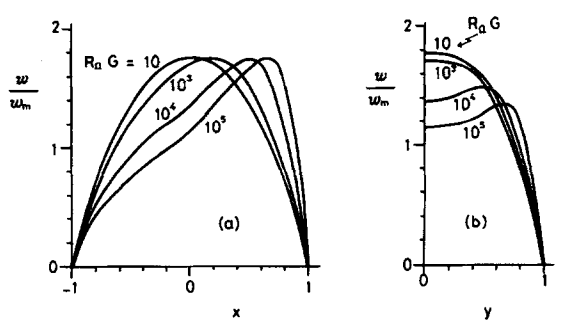

FIG. 8. Variation of the axial velocity profile (a) on the symmetric plane and (b) along the y axis with $R_\Omega G$ for $R_\Omega = 10$.

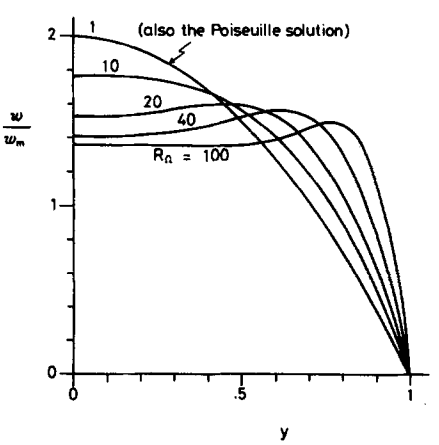

FIG. 9. Variation of the axial velocity profile along the y axis with R_Ω for $R_\Omega G = 10$.

$R_\Omega \gg R$ studied by Benton and Boyer. The third and fourth column of diagrams in Figs. 3 and 4 illustrate the transition from regime C to D, and then to B sequentially as $R_\Omega G$ increases for fixed values of R_Ω^2, with the pattern of Benton and Boyer on the top end and the pattern of Ito and Nanbu at the bottom. For $R_\Omega^2 = 10^4$, the location of ψ_{max} is shifted more toward the right from $\theta = 90°$ (regime C→D→B) than that for $R_\Omega^2 = 10^2$ (regime A→B) as $R_\Omega G$ increases. For example, the location of ψ_{max} can reach 81° for $R_\Omega^2 = 10^4$ but only reaches 85.5° for $R_\Omega^2 = 10^2$ according to Table I. The third and fourth row of diagrams in Figs. 3 and 4 illustrate similar transition from regime B to D and then to C as R_Ω^2 increases for fixed values of $R_\Omega G$. Further details of the above transitions can be seen from the data in Table I. For example, the locations of ψ_{max} shown in cases 30, 35, 36, 37, 38, and 43 of Table I indicate that the transition of the ψ pattern takes place continuously as R_Ω increases for $R_\Omega G = 10^5$, even though the contours shown in Fig. 4 for case $R_\Omega G = 10^5, R_\Omega = 20^2$ and $R_\Omega G = 10^5, R_\Omega^2 = 100^2$ are quite different.

Since the present flow patterns for various regimes had already been predicted qualitatively by the asymptotic solutions of Berman and Mockros,[7] it is helpful to see how accurate the asymptotic solution is as $R_\Omega G$ and R_Ω increase. Figure 10 shows $w_{m,LH}/w_{m,BM}$ and $\psi_{max,LH}/\psi_{max,BM}$ for different values of $R_\Omega G$ and R_Ω, where the properties with subscript LH denote the present calculation and those with subscript BM denote the results by Berman and Mockros. We found that the discrepancies between the two solutions are within 10% for w_m when $R_\Omega \leqslant 8$, $R_\Omega G \leqslant 1000$ and 20% for ψ_{max} when $R_\Omega \leqslant 5$, $R_\Omega G \leqslant 1000$.

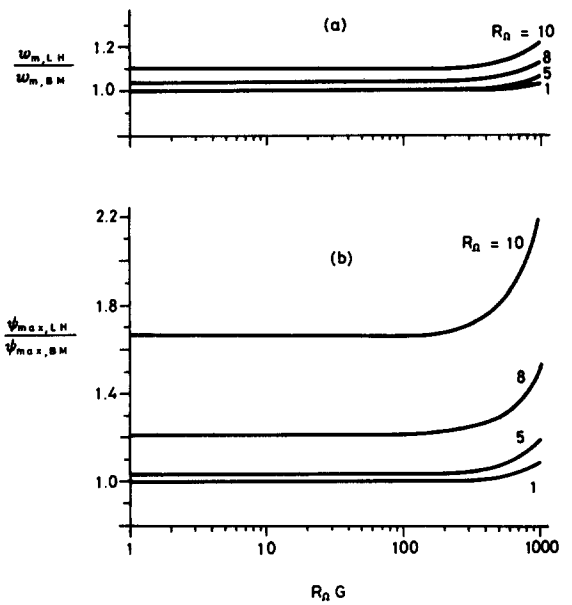

FIG. 10. Discrepancies between the present calculation and the perturbation solution by Berman and Mockros for different values of $R_\Omega G$ and R_Ω: (a) the mean axial velocity ratio $w_{m,LH}/w_{m,BM}$ and (b) the maximum streamfunction ratio $\psi_{max,LH}/\psi_{max,BM}$.

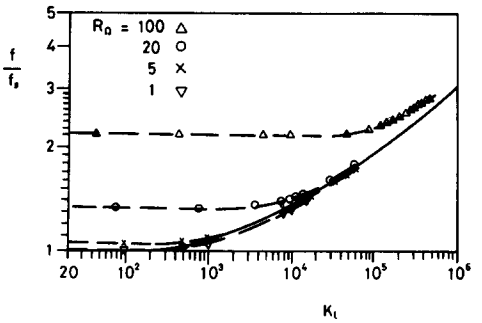

FIG. 11. Variation of the friction factor ratio (f/f_s) with R_Ω and K_l. The dashed lines show the present calculation. The solid line shows the experimental correlation by Ito and Nanbu.

D. The friction factor ratio (f/f_s)

As stated before, the present result for f/f_s agrees with the experimental correlation [Eq. (12a)] so that $f/f_s \approx F_\infty(K_l)$ when $R_\Omega/R < 0.25$ and $K_l > 220$. On the other hand, $f/f_s \approx F_0(R_\Omega)$ for small values of K_l according to the data in Table I. In general, f/f_s should be a function of both K_l and R_Ω. Such a relationship is plotted in Fig. 11 for $R_\Omega = 1, 5, 20$, and 100. We found that the data collapse onto the correlation curve as K_l increases but trace out different horizontal lines for different values of R_Ω when K_l is small. For any given value of R_Ω, the discrepancies between the data curve and the two legs (the horizontal line and the correlation curve) are within 10% according to the present calculation. For example, the values inside the parentheses in the last column of Table I are calculated based on Eq. (12a), even though the corresponding parameters are outside the range shown in Eq. (12b), but they are less than the corresponding numerical results by at most 5.5%. Hence the friction factor ratio can be approximated as

$$f/f_s = F_\infty(K_l), \quad K_l > K_{l*}, \tag{19a}$$

$$f/f_s = F_0(R_\Omega), \quad K_l \leqslant K_{l*}, \tag{19b}$$

where $K_{l*} = K_{l*}(R_\Omega)$ is the solution of $F_\infty(K_l) = F_0(R_\Omega)$, $F_\infty(K_l)$ is the right-hand side of Eq. (12a), and $F_0(R_\Omega)$ is determined by Eqs. (21a) and (21b) (see below). Equation (19a) and (19b) are valid within 10% error for the parameter ranges studied in this paper.

The horizontal lines which formed the left legs of the data curve in Fig. 11 according to Eq. (19b) may be regarded as the asymptotic solutions for $R_\Omega \gg R$. There are closed form solutions if we further let either $R_\Omega \gg 1$ or $R_\Omega \ll 1$. The former case is the asymptotic solution studied by Benton and Boyer[4] and Ito and Nanbu.[5] The result according to the integral analysis of Ito and Nanbu is

$$F_0(R_\Omega) = 0.1344 R_\Omega^{1/2}/(1 - 1.055 R_\Omega^{-1/2}), \quad \text{for } R_\Omega \gg 1, \ R_\Omega \gg R. \tag{20a}$$

The latter case may be obtained through the perturbation solution by Berman and Mockros. They obtained the volume flow rate in terms of the parameters G and R_Ω, which may be related to the mean velocity w_m' in this paper. On using Eqs. (8) and (9b), we obtained

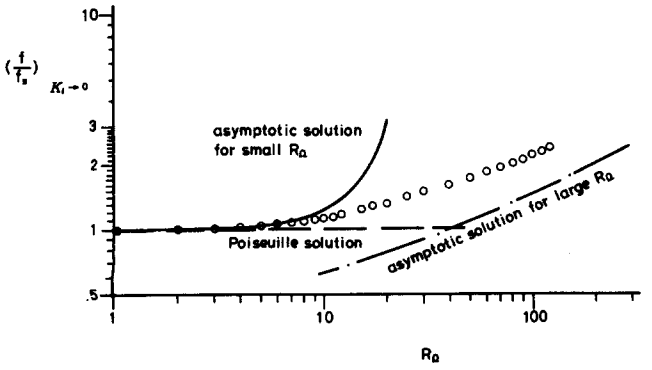

FIG. 12. Variation of the friction factor ratio (f/f_s) as $K_l = 8R_\Omega G \to 0$ with R_Ω. The circles represent the results of the present calculation.

$$F_0(R_\Omega) = (1 - R_\Omega^2/576)^{-1}, \quad \text{for} \quad R_\Omega \ll 1, \quad R_\Omega \gg R. \tag{20b}$$

Equations (20a) and (20b) are plotted in Fig. 12 together with the present numerical results. The numerical solution agrees with Eq. (20b) within 10% discrepancy for $R_\Omega \leqslant 11$ and diverges from it rapidly as R_Ω increases further. This is expected since the solution by Berman and Mockros[7] is based on small values of N_α ($= R_\Omega/48$). The numerical solution has a tendency to approach Eq. (20a), but it is unfortunate that we cannot carry out our numerical solution further for a larger value of R_Ω because of the limitation of the present numerical scheme. We expect that Eq. (20a) should underestimate the friction factor ratio since Ito and Nanbu did not take into account the fact that there exists an overshoot of the axial velocity along the y direction at the outer edge of the boundary layer as shown in Fig. 9. However, the asymptotic behavior that $f/f_s \sim R_\Omega^{1/2}$ for $R_\Omega \gg 1$ and $R_\Omega \gg R$ predicted by Eq. (20a) does agree with the scaling analysis. Also shown in Fig. 12 is the Poiseuille solution, which gives us a lower bound for the present calculation at small R_Ω. A correlation that fits the numerical data in Fig. 12 within 4% error is

$$R_\Omega^{-1/2}(f/f_s) = 0.9655 R_\Omega^{-0.4368}, \quad 1 \leqslant R_\Omega \leqslant 12, \tag{21a}$$

$$R_\Omega^{-1/2}(f/f_s) = 0.5338 R_\Omega^{-0.1946}, \quad 12 \leqslant R_\Omega \leqslant 120. \tag{21b}$$

E. Compare with Duck's result

Duck carried out numerical solutions for cases 4, 7, 9, 10, and 11 in Table I via a Fourier decomposition method. Figure 13(a) compares the present result with Duck's for case 4 ($R_\Omega = 1$, $R_\Omega G = 1000$). The values for the contours labeled in the figure [also those in Figs. 13(b) and 14] are Duck's dimensionless axial velocity and secondary streamfunction. Recall that the flow pattern should be symmetric about $y = 0$, so that the present result and Duck's result are plotted inside the upper and lower semicircle, respectively, in the figure for comparison. The agreement is fair for both the streamfunction contours and the values of maximum axial velocity, but the axial velocity contours are quite different from each other. For example, w_{max} occurs at (0.25,0°) in the present calculation instead of near the origin according to Duck's result. However, the present result does agree fairly with the perturbation solution by Berman and Mockros, as shown in Fig. 13(b). The scaling analysis according to either Eq. (15a) or (16a) indeed shows that the convection term is not negligible, which implies that the axial velocity profile should be somewhat different from that of the Poiseuille flow. For larger values of R_Ω and $R_\Omega G$, the discrepancies of the axial velocity profiles between the present result and Duck's grow such that they look as if they are completely different flow patterns. Figures 14(a) and 14(b) show the comparison for case 9 ($R_\Omega = 5$, $R_\Omega G = 25\,000$) and case 11 ($R_\Omega = 5$, $R_\Omega G = 75\,000$). The present calculations indicate that the axial velocity profiles are skewed toward the pressure side with one maximum occurring along the symmetric plane, which belong to regime B defined before in Sec. IV C. Duck's results show that there are two maxima along the symmetric plane and the flow pattern in Fig. 14(a) belongs to regime C instead of B. Despite the

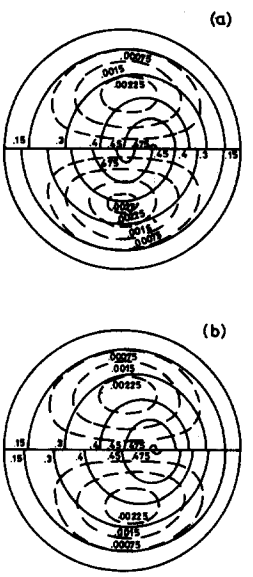

FIG. 13. A comparison of the various results for $R_\Omega = 1$ and $R_\Omega G = 1000$. The axial velocity and the secondary streamfunction contours are represented by solid and dashed lines, respectively. (a) The present calculation (upper) versus Duck's calculation (lower); (b) the present calculation (upper) versus the perturbation solution by Berman and Mockros (lower).

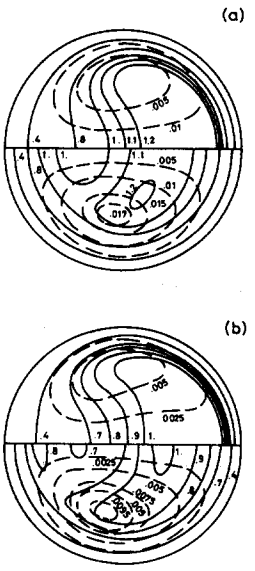

FIG. 14. Comparison between the present calculations (upper) and Duck's results (lower) for (a) $R_\Omega = 5$, $R_\Omega G = 25\,000$ and (b) $R_\Omega = 5$, $R_\Omega G = 75\,000$. The axial velocity and the secondary streamfunction contours are represented by solid and dashed lines, respectively.

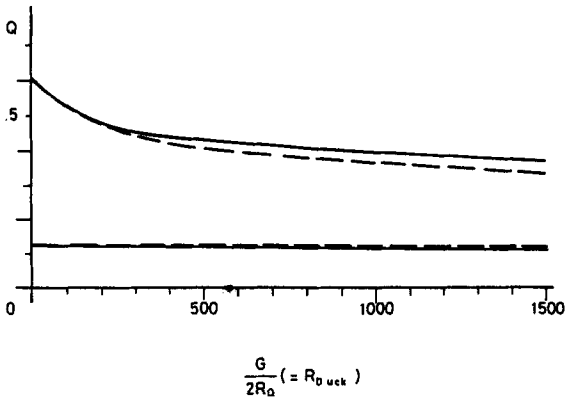

FIG. 15. A comparison of the dimensionless volume flow rate Q between the present results (solid lines) and Duck's results (dashed lines) for $R_\Omega = 1$ (the lower two curves) and 5 (the upper two curves).

above discrepancies for the detailed flow structure, the dimensionless volume flow rate (Q) according to Duck's definition for both Duck's and the present result agree with each other within 10%, as shown in Fig. 15. Since the friction factor f is proportional to Q^{-2}, Duck's result for f also agrees with the experimental correlation in Eq. (12a) within 21% error according to the data shown in Table I and Fig. 15. One possible explanation for the discrepancies in Fig. 14 is that bifurcation occurs such that dual solutions exist for those cases. Both the present result and Duck's result could be the solution of the present problem. Since $R_\Omega/R = O(10^{-2})$, the cases studied in Fig. 14 should be similar to the curved pipe flow problem studied by Collins and Dennis[10] and Dennis and Ng.[13] The method employed by Dennis and Ng was basically the same as that in Duck's and they found dual solutions for the same cases studied by Collins and Dennis, who found only one solution. Note that the present analysis employed basically the same method as that in Collins and Dennis. However, Dennis and Ng found that their secondary flow has a four-vortex pattern consisting of two symmetrical vortex pairs, but Duck's secondary flow consists of only a symmetrical pair of counter-rotating vortices of the Taylor–Goertler type as the present study, which seems to rule out the above possibility for dual solutions. Anyway, further investigations are required for a better understanding of the bifurcation problem for the present flow system.

V. CONCLUSION

By comparing the scaling results in Sec. IV C with the detailed numerical results in Table I and Figs. 3 and 4, we found that there are four types of flow regimes, depending on the relative magnitudes of the dimensionless parameters R_Ω and $R_\Omega G$. (i) When $R_\Omega < 10$ and $R_\Omega G < 100$, the secondary flow is too weak to modify the main flow such that the axial velocity profile is essentially axisymmetric and parabolic with the maximum value occurring at the pipe center; (ii) when $R_\Omega < 0.85(R_\Omega G)^{1/3}$ and $R_\Omega G > 100$, the convection effect resulting from the secondary flow modifies the axial velocity profile and shifts its maximum value toward the pressure side ($x > 0$) along the symmetric plane; (iii) when $R_\Omega > 1.26(R_\Omega G)^{2/5}$ and $R_\Omega > 10$, the Coriolis force dimples the axial velocity profile at the center and creates a dumbbell-like profile with two maxima along the y axis, one along the positive axis and one along the negative axis; and (iv) when $0.85(R_\Omega G)^{1/3} \leqslant R_\Omega \leqslant 1.26(R_\Omega G)^{2/5}$ and $R_\Omega G > 100$, both mechanisms in (ii) and (iii) affect the axial velocity profile and make it skew toward the pressure side with two maxima, which occur symmetrically on both sides of the symmetric plane. It is the transition regime between (ii) and (iii). The transition takes place smoothly for the above four regimes. These four regimes had already been predicted qualitatively by the Berman and Mockros[4] perturbation solution. The parameter ranges that are covered by the present study are large enough that they bridge most of the previous asymptotic analyses. Based on the present calculations, the friction factor ratio between the rotating and stationary pipe flow can be approximated by Eqs. (19a) and (19b) within 10% error for most of the laminar regime of engineering interest.

[1] S. A. Berger, L. Talbot, and L. S. Yao, Annu. Rev. Fluid Mech. **15**, 461 (1983).
[2] S. N. Baura, Proc. R. Soc. London Ser. A **227**, 33 (1954).
[3] G. S. Benton, J. Appl. Mech. **23**, 123 (1956).
[4] G. S. Benton and D. Boyer, J. Fluid Mech. **26**, 69 (1966).
[5] H. Ito and K. Nanbu, J. Basic Eng. **93**, 383 (1971).
[6] P. W. Duck, Phys. Fluids **23**, 614 (1983).
[7] J. Berman and L. F. Mockros, J. Fluid Mech. **144**, 297 (1984).
[8] K. Mansour, J. Fluid Mech. **150**, 1 (1985).
[9] W. D. Morris, *Heat Transfer and Fluid Flow in Rotating Coolant Channels* (Wiley, New York, 1981), Chap. 6.
[10] W. M. Collins and S. C. R. Dennis, Q. J. Mech. Appl. Math. **28**, 133 (1975).
[11] L. Fox, Proc. R. Soc. London Ser. A **190**, 31 (1947).
[12] C. H. Hsu, Master's thesis, Institute of Applied Mechanics, National Taiwan University, 1988.
[13] S. C. R. Dennis and M. Ng, Q. J. Mech. Appl. Math. **35**, 405 (1982).